Modeling and simulation of inertial drop break-up in a turbulent pipe flow downstream of a restriction

Riccardo Maniero [a,c], Olivier Masbernat [a,c], Eric Climent [b,c,*], Frédéric Risso [b,c]

[a] *Laboratoire de Génie Chimique, Université de Toulouse (INPT-UPS), CNRS, 4 Allée Emile Monso, Toulouse 31432 cedex 4, France*
[b] *Institut de Mécanique des Fluides, Université de Toulouse (INPT-UPS), CNRS, Allée du Professeur Camille Soula, Toulouse 31400, France*
[c] *Fédération de recherche FERMaT, CNRS, Toulouse, France*

ABSTRACT

This work deals with the modeling of drop break-up in an inhomogeneous turbulent flow that develops downstream of a concentric restriction in a pipe. The proposed approach consists in coupling Euler–Lagrange simulations of the drop motion to an interface deformation model. First the turbulent flow downstream of the restriction is solved by means of direct numerical simulation. Single drop trajectories are then calculated from the instantaneous force balance acting on the drop within the turbulent field (one-way coupling). Concurrently, the interface deformation is computed assuming the drop to behave as a Rayleigh–Lamb type oscillator forced by the turbulent stress along its trajectory. Criterion for break-up is based upon a critical value of drop deformation.

This model has been tested against experimental data. The flow conditions and fluids properties have been chosen to match those experimental investigations. Both turbulent flow statistics and break-up probability calculations are in good agreement with experimental data, strengthening the relevance of this approach for modeling break-up in complex unsteady flow.

1. Introduction

Predicting drop or bubble break-up in complex flows (i.e. unsteady, heterogeneous, high concentration) is a major issue in many industrial applications such as crude oil transport, liquid–liquid extraction, and bubble columns. Modeling break-up means answering two basic questions: the occurrence of break-up and the resulting distribution of fragments. These two problems are generally addressed through a Weber number, ratio between the statistically averaged pressure force at the scale of the drop (or bubble) that tends to deform it, and the surface tension force that tends to restore the particle shape to the spherical form. In average, the greater the mechanical energy input, the greater the break-up rate and the finer the size distribution (see for instance Galinat et al., 2005). Modeling based on average turbulent intensity proved to be efficient when the turbulence is intense enough to induce a large break-up rate (Martínez-Bazán et al., 1999; Lasheras et al., 2002). However, since this approach ignores the dynamic response of the drop (or bubble) to a local instant forcing of the flow, it cannot properly describe the break-up mechanisms when the residence time of the drop before break-up is not short compared to the time scale of the interface deformation (Risso and Fabre, 1998). This limits the range of validity of break-up models based on an average critical Weber number in time-dependent, non deterministic and inhomogeneous flows.

The development of breakage scaling laws in turbulent flows thus also requires the coupling between the drop deformation dynamics with those of the local flow stress. This type of approach has been successfully applied to predict bubble deformation statistics in a homogeneous turbulence (Risso and Fabre, 1998) and drop break-up probability in an inhomogeneous turbulent flow (Galinat et al., 2007a). In the limit of weak deformations, the drop is considered as a linear damped oscillator forced by the external pressure field at the scale of the drop. In this framework, the criterion for break-up is based upon maximum amplitude of the drop deformation instead of a maximum of the instantaneous external forcing (or critical Weber number). In order to use this model, the characteristic time scales of the drop (oscillation proper frequency and damping rate) and the local instantaneous stress field in the flow must be known. The two first parameters can be obtained for bubbles from potential flow theory (Lamb, 1932) and for drops in liquids from linearized Navier–Stokes equations approximation (Miller and Scriven, 1968; Prosperetti, 1980). Note that the presence of surfactants may drastically change these two time scales (Lu and Apfel, 1991; Abi Chebel, 2009). The external stress seen by the drop can be either deduced from flow measurements (Galinat et al., 2007b) or calculated by numerical simulations.

* Corresponding author at: Institut de Mécanique des Fluides, Université de Toulouse (INPT-UPS), CNRS, Allée du Professeur Camille Soula, Toulouse 31400, France.

E-mail address: eric.climent@imft.fr (E. Climent).

This work is based on this approach. We present a numerical study of break-up probability of oil drops in an inhomogeneous turbulent flow of an aqueous phase. The flow configuration considered here is the same as that experimentally studied by Galinat et al. (2007b). It is a flow downstream of a concentric orifice in a vertical pipe. In the range of Reynolds numbers studied, the flow is turbulent and spatially inhomogeneous downstream of the orifice. Drops are injected upstream of the orifice and their probability of break-up is measured in a finite pipe volume above the orifice. The flow field is calculated via direct numerical simulation (DNS) and the drop motion is calculated from a Lagrangian tracking method (one-way coupling). Following the drop trajectory, drop deformation is calculated by solving a forced dynamic oscillator the response of which provides a criterion for break-up occurrence. Statistical averaging of break-up events leads to a break-up probability. Numerical results are discussed and compared to experimental data.

2. Flow configuration and breakup modeling

The flow test section investigated by Galinat et al. (2007b) is a vertical pipe of internal diameter $D = 0.03$ m equipped with a concentric orifice of diameter $D_o = 0.015$ m ($\beta = D_o/D = 1/2$). This restriction generates an upward turbulent jet flow which develops downstream over few pipe diameters (Fig. 1). The two-liquid phase system consists of an aqueous solution of glycerin as the carrying phase and colored n-heptane as the drop phase. Densities of drop and continuous phases, ρ_d and ρ_c, as well as viscosities, μ_d and μ_c, and interfacial tension σ are provided in Table 1.

Individual drops of 2–3 mm diameter are injected in the flow a few pipe diameters upstream of the orifice (where the flow is laminar and the drop is weakly deformed). Drop trajectories have been recorded with the help of a high-speed camera at 500 fps. Drop break-up locations in the flow field downstream of the orifice have been recorded at different flow rates and drop diameters. A typical map of break-up locations is reported in Fig. 4 (white crosses). Video recordings showed that, for the case studied ($U_o = 0.6$ m s^{-1} and $d = 2.4$ mm), break-up occurrence was limited to a flow region bounded by $x/D = 1$ and $x/D = 2$ ($x = 0$ corresponds to the orifice plane in Fig. 1).

Galinat et al. (2007b) have measured the velocity field of the continuous phase using high-speed PIV in a median plane of the
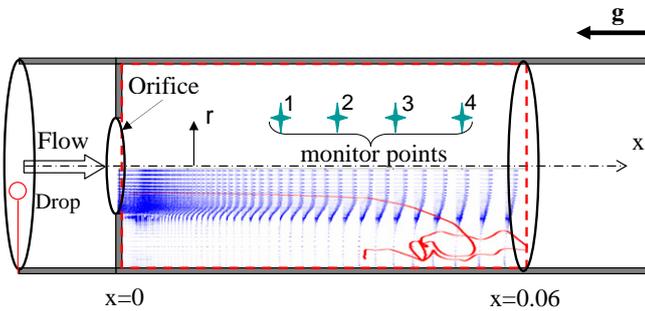

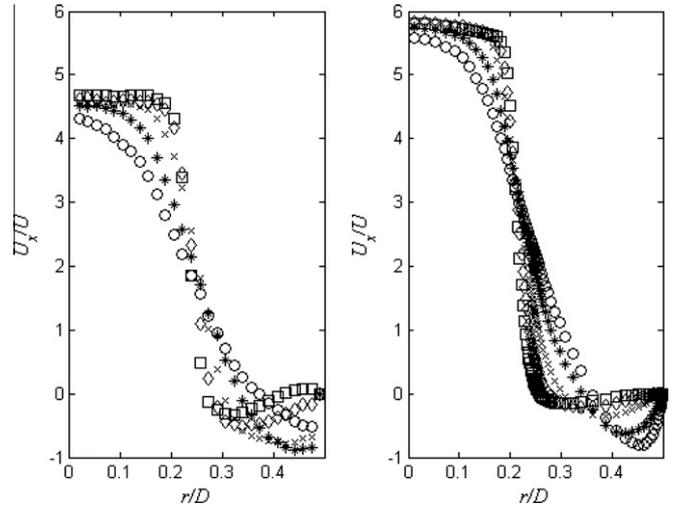**Fig. 2.** Radial velocity profiles downstream of the orifice of mean axial velocity U_x: □ ($x/D = 1/3$), ◇ ($x/D = 2/3$), × ($x/D = 1$), ∗ ($x/D = 4/3$), ○ ($x/D = 5/3$). Left: experiments; right: simulations.

pipe, for two mean velocities U_o through the orifice, 0.6 and 0.9 m/s, with uniform spatial and time resolutions of 0.55 mm and 0.5 m s respectively. The investigated flow region extends from the orifice to 0.06 m downstream ($x/D = 2$). Averages have been computed assuming the flow to be axisymmetric. Radial profiles of mean and fluctuating axial velocity at different distances from the orifice are illustrated in Figs. 2 and 3. The flow field produced downstream of the orifice is highly heterogeneous: it consists of a central jet with a flat velocity profile and strong recirculation patterns around it, which develops as the distance from the orifice is increased. The numerical investigation (presented in Section 3) is restricted to the case $U_o = 0.6$ m s^{-1} ($U = 0.15$ m s^{-1}), corresponding to $Re_o = \rho_c U_o D_o/\mu_c = 2100$ ($Re = \rho_c U D/\mu_c = 1050$).

A global estimation of the dissipation rate produced by the orifice in the whole test section can be obtained from the pressure difference between the orifice and two diameters downstream,

$$< \varepsilon > \cong \frac{1}{C_{do}^2}(1 - C_{do}^2)(1 - \beta^2)(1/\beta^4 - 1)\frac{U^3}{4D} \cong \frac{U^3}{D}, \qquad (1)$$

Fig. 1. Scheme of the flow test section and simulation domain ($x/D = -2.5$ up to $x/D = 10$). Locations of monitor points 1, 2, 3 and 4 are respectively: $r/D = 0.25$ and $x/D = 0.82$, 1.09, 1.36 and 1.68.

Table 1
Fluids properties at 20 °C.

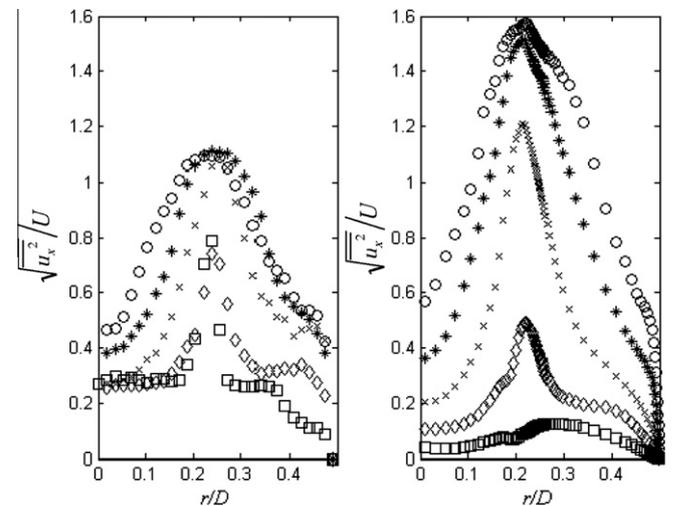| Liquid phase	ρ (kg m^{-3})	μ (Pa s)	σ (N m^{-1})
Water–glycerin (cont.)	1100	4.7×10^{-3}	23.6×10^{-3}
Colored heptane (disp.)	683.7	4.5×10^{-4}	

Fig. 3. Profiles of axial velocity fluctuations r.m.s. downstream of the orifice. □ ($x/D = 1/3$), ◇ ($x/D = 2/3$), × ($x/D = 1$), ∗ ($x/D = 4/3$), ○ ($x/D = 5/3$). Left: experiments; right: simulations.

where $\beta = D_o/D = 1/2$ is the orifice ratio and the discharge coefficient C_{do} is about 0.85 in that range of Reynolds number (Galinat et al., 2005). Also, from Figs. 2 and 3, a global value of the velocity fluctuation over the whole flow can be reasonably estimated to

$$u' = \langle \sqrt{\overline{u_x^2}} \rangle \sim 0.5U, \qquad (2)$$

(u_x being the instant velocity fluctuation in x direction, brackets' symbol indicating the spatial average in a pipe volume of $2D$ length and over bar symbol time average). Assuming the dissipation rate downstream of the orifice is due to turbulence, the integral length scale corresponding to an isotropic turbulent field would be

$$\Lambda \cong D \frac{(3/2)^{3/2}(u'/U)^3 4C_{do}^2}{(1 - C_{do}^2)(1 - \beta^2)(1/\beta^4 - 1)} \cong 0.2D = 0.4D_o = 6 \text{ mm}. \qquad (3)$$

In the same way, Taylor micro-scale λ and Kolmogorov scale η can be derived from *r.m.s.* velocity and dissipation rate downstream of the orifice: $\lambda \cong 2.5 \frac{D}{\sqrt{Re}} \cong 2.3$ mm and $\eta \cong DRe^{-3/4} \cong 0.16$ mm at $Re = 1050$, which leads to

$$Re_\lambda \cong 40 \text{ and } \frac{d}{\eta} > 10, \qquad (4)$$

for drop diameters larger then 2 mm.

These estimated turbulent length scales indicate that the considered drop diameter lies in the inertial subrange of turbulence, the spectral width of which being limited due to the rather low value of Re_λ.

Due to the inhomogeneous nature of the turbulent jet flow downstream of the orifice, several contributions to the external forcing applied to a traveling drop needs to be evaluated. Following Kolmogorov–Hinze theory (Kolmogorov, 1949, Hinze, 1955), the time average turbulent Weber number is defined at any position vector $\mathbf{x}$ as

$$We = \frac{\rho_c \overline{\delta u^2(x,d)} d}{\sigma}, \qquad (5)$$

where $\overline{\delta u^2(x,d)}$ is the mean square of the flow velocity fluctuation difference over a distance equal to the drop diameter d (overbar denotes time averaging). It is also the trace of the 2nd order structure function of the Reynolds stress tensor at a distance equal to the drop diameter d, which in the case of isotropic turbulence, is simply proportional to the longitudinal structure function of the velocity (see Monin and Yaglom, 1975). At each location $\mathbf{x}$ of the flow downstream of the orifice, the Eulerian quantity $\overline{\delta u^2(x,d)}$ has been calculated as follows

$$\overline{\delta u^2(x, d_\alpha)} = \max_\alpha \left\{ [u_x(x + \mathbf{d}_\alpha/2) - u_x(x - \mathbf{d}_\alpha/2)]^2 + [u_r(x + \mathbf{d}/2) - u_r(x - \mathbf{d}_\alpha/2)]^2 \right\}, \qquad (6)$$

where vector $\mathbf{d}_\alpha$ (of norm d) is oriented according four different angular position α with respect to Ox axis ($0°, 45°, 90°, -45°$), u_x and u_r being respectively the velocity fluctuations in axial and radial directions. The Weber number considered in (5) is computed from the maximum value of the structure function among these four different orientations.

Another inertial contribution is provided by the mean flow deceleration in the flow direction due to the restriction, $\partial U_x / \partial x$. The Weber number associated with this inertial stress reads

$$We_U = \rho_c \left(\frac{\partial U_x}{\partial x} \right)^2 \frac{d^3}{4\sigma}. \qquad (7)$$

The relative velocity between the drop and the fluid, $U_t = |v - u|$, is an additional source of inertial contribution to the drop deformation. For a 2.4 mm diameter drop, U_t is about 8.7 cm/s ($Re_t = \frac{\rho_c U_t d}{\mu_c}$
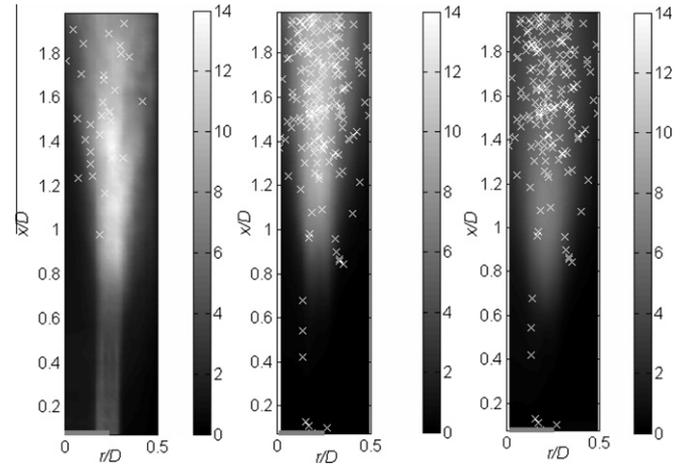

Fig. 4. Spatial distribution of the average turbulent Weber number. White crosses correspond to locations where drop break-up occurs. Left: turbulent Weber number evaluated from experimental data and Eq. (5) – center: turbulent Weber number evaluated from numerical data and Eq. (5) – right: turbulent Weber number evaluated from numerical data and Eq. (15).
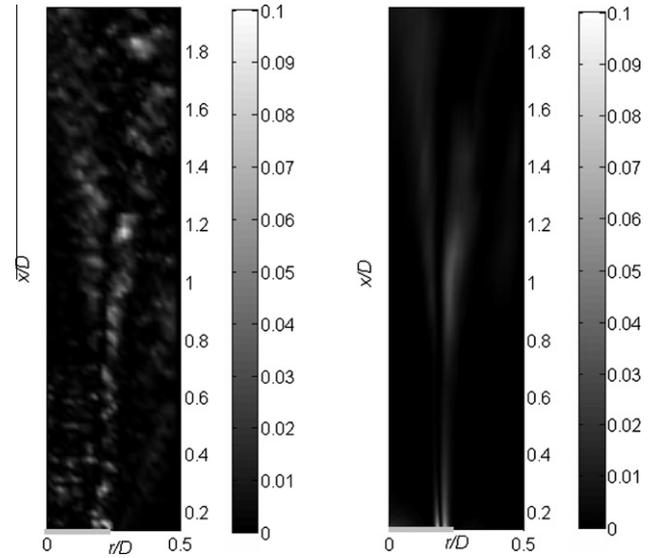

Fig. 5. Spatial distribution of the Weber number associated with average flow acceleration (Eq. (7)). Left: experiments; right: simulation.

≈ 50) and the corresponding Weber number $We_t = \frac{\rho_c U_t^2 d}{\sigma}$ is about 0.8.

The jet flow through the orifice leads to the development of strong mean velocity gradients in the transverse plane (see Fig. 2). Those involve a viscous stress the contribution of which can be expressed via the Capillary number

$$Ca = \mu_c \frac{\partial U_x}{\partial r} \frac{d}{2\sigma}. \qquad (8)$$

The turbulent Weber number (Eqs. (5) and (6), Fig. 4), the Weber number associated with the inertial stress (Eq. (7), Fig. 5) and the capillary number (Eq. (8), Fig. 6), have been calculated from both PIV measurements and simulation data for a drop of 2.4 mm diameter. The agreement is correct, both qualitatively and quantitatively. Note that some discrepancies on the spatial distribution of the Weber number associated with inertial stress (Fig. 5) might be due to the lack of convergence of experimental
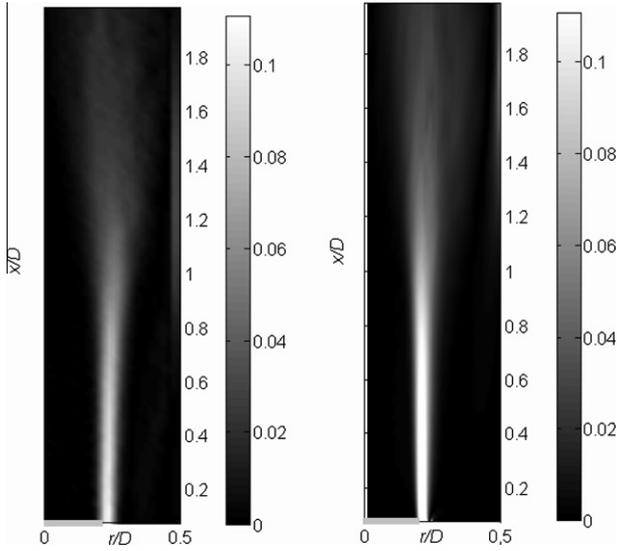
Fig. 6. Spatial distribution of the capillary number (Eq. (8)). Left: experiments; right: simulation.

averages. These results show that for the flow case studied, the contribution of turbulence to the deformation (Eq. (5), Fig. 4) is about 2 orders of magnitude larger than that of the mean flow (Eq. (7), Fig. 5 and Eq. (8), Fig. 6) and an order of magnitude larger than the contribution of mean slip velocity $We_t = \rho_c U_t^2 d/\sigma \sim 0.8$. Note however that drop axial acceleration in the entry section due to the restriction is not considered in the inertial Weber number calculated in the downstream field (Eq. (7)). It can be estimated considering that the entering flow upstream of the orifice is accelerated from U (mean velocity in the pipe) to U_o (mean velocity in the orifice) over a distance equal to the orifice diameter D_o

$$\left(\frac{\partial U_x}{\partial x}\right)_{x=0} \cong \frac{U_o - U}{D_o} = \frac{U_o}{D_o}(1 - \beta^2) = 0.75 \frac{U_o}{D_o} = 30 \text{ s}^{-1}. \quad (9)$$

The corresponding Weber number (Eq. (7)) equals 0.14 and can be also neglected compared to the turbulent stress Weber number (Eq. (5)).

As a consequence, in the whole domain downstream of the orifice, the external forcing responsible of drop deformation along its trajectory (Eq. (12)) can be scaled using an instantaneous Weber number

$$We(\mathbf{x}(t), d) = \frac{\rho_c \delta u^2(X(t), d)d}{\sigma}, \quad (10)$$

where u is the instantaneous flow velocity fluctuation seen by the drop along its trajectory and $\mathbf{X}(t)$ is the position vector of the drop center of mass at current time t and

$$\delta u^2(X(t), d_\alpha) = \max_\alpha \left\{ [u_x(X(t) + \mathbf{d}_\alpha/2) - u_x(X(t) - \mathbf{d}_\alpha/2)]^2 \right.$$
$$\left. + [u_r(X(t) + \mathbf{d}/2) - u_r(X(t) - \mathbf{d}_\alpha/2)]^2 \right\}. \quad (11)$$

The shape of a drop can be described as the sum of the n first spherical harmonics (see examples in Risso, 2000). Each of them is associated to a dynamical mode with its own eigenfrequency f_n and damping rate β_n. Provided that the Weber number is not too large, Risso and Fabre (1998) showed that large-amplitude deformations leading to breakup in a turbulent flow essentially involve axisymmetric spherical harmonics of mode 2, which correspond to a lengthening or flattening of the drop shape. Using the drop diameter d as length scale and $1/2\pi f_2$ as time scale, this model reads in dimensionless form

$$\frac{d^2 \widetilde{A}_2}{d\tilde{t}^2} + 2\xi \frac{d\widetilde{A}_2}{d\tilde{t}} + \widetilde{A}_2 = K \frac{\rho_c \delta u^2 d}{\sigma} = KWe(X(\tilde{t}), d). \quad (12)$$

The drop deformation can thus be characterized by the amplitude A_2 of mode 2 and calculated as a function of time (i.e. following the drop trajectory) by computing the dynamic response of a linear oscillator to the instantaneous turbulent forcing. It is assumed here is that Eq. (12) describes the energy transfer from turbulence to mode 2. Other modes are also excited but their contribution to the large-scale deformation of the drop is lower for two reasons: first, the turbulence spectrum contains less energy at the characteristic length and time scales of higher order modes. Second, since those involve smaller wavelengths, these modes induce deformation at smaller scales. This assumption of the predominance of mode 2 is consistent with the original assumption by Kolmogorov and Hinze that the breakup of a drop is dominated by the turbulent scales at the size of the drop. This is supported by the observations made by Risso and Fabre (1998) and Galinat et al. (2007a,b). In Eq. (12), the tilde symbol denotes non-dimensional variables and $\xi = \beta_2/(2\pi f_2)$ is the damping rate coefficient. The left-hand side of Eq. (12) describes the dynamics response of the drop shape amplitude to the turbulent forcing (right-hand side). The frequency f_2 and the damping rate β_2 for any arbitrary Reynolds numbers were first derived by Miller and Scriven (1968) and by Prosperetti (1980). Here, we use the asymptotic expressions proposed by Lu and Apfel (1991) for low-viscosity fluids and valid in the present case. Those give $f_2 = 43$ Hz and $\beta_2 = 32 \text{ s}^{-1}$.

The model proposed in Eq. (12) accounts for the spatial structure of the turbulence at the scale of the drop, suggesting that the scaling coefficient K should not depend strongly on the nature of the flow. However this is still an open question that should be solved by investigating different types of flow. Is worth recalling that the original Kolmogorov–Hinze idea was to consider average pressure fluctuations at the drop scale and was restricted to isotropic turbulence. There is no straightforward method to adapt this concept to non-isotropic turbulence and instantaneous fluctuations. Here we decided to use the maximum of the square velocity difference over eight directions in the radial–axial plane to allow quantitative comparisons with the experimental study of Galinat et al. (2007a,b). However, considering the maximum over a larger number of directions or accounting for the azimuthal velocity component will have only changed slightly the value of K, which can be, in all cases, identified knowing one value of A_2 at a given time during deformation and break-up process.

3. Numerical simulation of the carrying flow and turbulence description

3.1. Description of simulation parameters

The flow of the continuous phase has been simulated by direct numerical simulation (DNS) of the unsteady three-dimensional Navier–Stokes equations in the same flow geometry and at the same flow rate as in the experiments ($U = 0.15 \text{ m s}^{-1}$ or $U_o = 0.6 \text{ m s}^{-1}$). The DNS technique is based on the solution of Navier–Stokes equations without any statistical modeling of turbulence. All the length and time scales of the turbulent flow are resolved by temporal integration and mesh refinement. The fluid is considered as Newtonian and incompressible with constant physical properties (fluid density and dynamic viscosity). The unsteady three-dimensional Navier–Stokes equations are solved in cylindrical coordinates. These equations are solved using a conservative finite-volume method. Primitive variables (velocity $\mathbf{u}$ and pressure P) are located on a staggered non-uniform Cartesian grid. Spatial derivatives are computed with second-order accuracy. Temporal
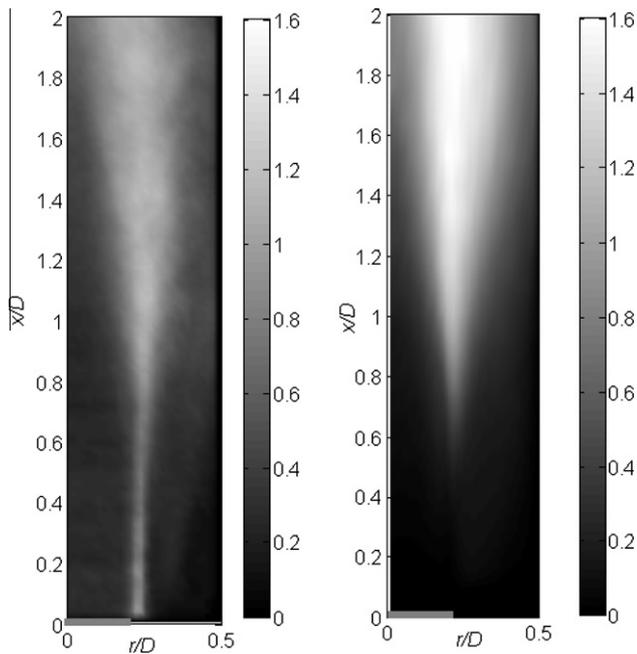
Fig. 7. Spatial distribution of axial velocity fluctuations *r.m.s.* Left: experiments; right: simulation.

Fig. 8. Power spectral density of the axial velocity: simulations (thin line) and experiments (thick line). (a) point 1; (b) point 2 (see Fig. 1 for location of points 1 and 2).

integration is achieved through a third-order Runge–Kutta scheme and a semi-implicit Crank–Nicholson scheme for the viscous terms. Flow incompressibility is met by using an auxiliary potential for the projection method leading to a Poisson equation for the pressure correction. The corresponding simulation code has been widely used and validated under laminar and turbulent flow regimes using either direct numerical simulations or large eddy simulations for higher Reynolds turbulence (e.g. Merle et al., 2005, and references therein). In the present study no sub-grid modeling has been used while all the turbulence features are fully resolved (mesh stretching is used close to the orifice to capture strong velocity gradients). On the pipe and orifice walls, no-slip boundary conditions are imposed. The flow is driven by constant pressure drop along the pipe while an outlet boundary condition is applied at the pipe exit.

The simulation domain, which extends towards $x/D = 10$, has been meshed in cylindrical coordinates, with 120 nodes in axial direction x, 80 in radial direction r and 32 in angular direction θ. The grid is equally spaced in the angular direction while it has been stretched in radial and axial directions near the circular orifice, to resolve regions of high shear and the downstream turbulent structures. At the inlet $x/D = -2.5$, a Poiseuille velocity profile is imposed assuming the flow to be laminar while the outlet is modeled by a numerical condition of free fluid exit. The inflow pipe Reynolds number is equal to 1050 (based on pipe diameter, mean flow rate and fluid viscosity). Upstream of the orifice, the flow is purely streamwise but the presence of a sudden reduction of section induces radial components of the velocity field yielding closed streamlines. The flow accelerates when crossing the orifice section and leads to the formation of a jet confined by the pipe walls. A long recirculation zone follows the orifice, increasing with Reynolds number (Morrison et al., 1993). The flow remains steady for low to moderate Reynolds number, and the spatial extension of the toroidal vortex obtained in the simulations has been compared to experiments (Macagno and Hung, 1967) with good agreement. The pressure drop has been compared to classic empirical correlations as well. Beyond $Re_o = 1600$, the flow becomes unsteady (large scale periodic oscillations characterized by a Strouhal number roughly constant and equal to 0.5, in good agreement with Becker and Massaro, 1968). When the flow is unsteady, the recirculation
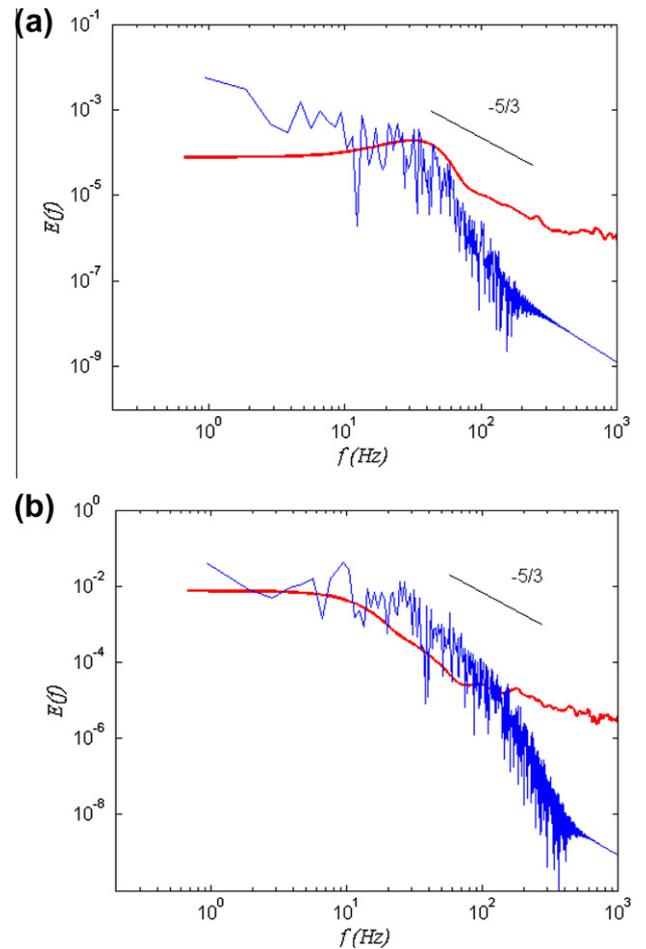
zone shrinks drastically and eventually increases again in the range $Re_o = 2100$. The central jet generated through the orifice becomes gradually turbulent while large scale structures are controlled by the oscillation of the recirculation zone. The simulation domain has been chosen long enough to capture all these features.

3.2. Flow simulation results

Simulation results have been compared to PIV measurements (see in Fig. 1 the window of experimental measurements). In Fig. 2, experimental and numerical profiles of the average axial velocity U_x at several locations downstream of the orifice are displayed. Both results are scaled by the pipe cross-sectional velocity U. These profiles show the gradual spreading of the jet and the existence of a recirculation zone. One can observe a significant overestimation of the calculated mean axial velocity profiles in the core of the jet, which results from an underestimation of the backflow in the region comprised between the orifice and the pipe wall. Based on a simple mass balance consideration, it can be shown that an underestimation of the backflow equal to 5% of the velocity in the orifice U_o, induces an overestimation of 21% of U_o in the jet core.

Profiles of the *r.m.s.* of axial velocity fluctuations are compared in Fig. 3. Here again, significant differences between experimental and numerical data are observed. Those are directly related to the presence of low frequency oscillations of the jet (that can be

detected in the power spectral density graph of Fig. 8a). These oscillations can't be present numerically since upstream of the orifice, the flow is laminar and does not contain any excitation modes of such oscillations. A simulation test have been carried out by superimposing small amplitude random noise (<0.5% U) to the upstream flow, resulting in a dramatic increase of turbulence and recirculation downstream of the orifice, which did not compare favorably with the experimental data. This test has shown the extreme sensitivity of the flow pattern downstream of the orifice to the inlet conditions and the probable role of self-sustained oscillations. Such large scale instability of the flow has been characterized experimentally (Furuichi et al., 2003). A steady symmetry breaking bifurcation in the flow through a 1:2 sudden axisymmetric expansion (Mullin et al., 2009) has been observed for Reynolds numbers ranging from 1150 to 1500. Further increase of the Reynolds leads to intermittent bursts which eventually results in flapping oscillations of the reattachment shear layer. These low frequency fluctuations are responsible for the high fluctuation level observed in the experiments at distances smaller than $x/D = 1$ and possibly act as promoters of turbulence which develops more rapidly (i.e. at a smaller distance from the orifice), in the experiments than in the numerical simulations. As a result, below one diameter downstream of the orifice, the fluctuation level in the experiments is larger than in the simulations whereas above $x/D = 1$, the trend is reversed. Temporal energy spectra of the axial velocity (Fig. 8a–b) shed some light on this feature. The energy spectra of the axial velocity have been scaled by the square of the average axial velocity. The experimental spectra extracted from PIV measurements have been smoothed by applying the Welch windowing method. The experimental spectrum at point 1 has a clear bump around $f = 4$ Hz which disappears downstream (point 2). Due to the exact steady Poiseuille flow inlet condition, such a large-scale oscillation of the jet does not arise from the simulations. This has an impact on the velocity fluctuations close to the orifice and as a consequence, the profile of the average velocity is stiffer in the experiments than in the simulation. Finally, this phenomenon is damped and a good agreement is achieved beyond $x/D = 1$.

Although the turbulence is inhomogeneous and anisotropic, the energy spectra from PIV measurements exhibit a clear inertial subrange characterized by the classical $-5/3$ power law. The power law of the inertial subrange in the energy spectrum is also confirmed in simulations up to the frequency 2×10^2 Hz. For higher frequencies an increase of the slope is observed and may be related to the progressive coarsening of the grid, which filters the smallest scales. In the region of interest where we intend to compare experiments and numerical prediction of drop break-up, the spatial and temporal resolutions seem to be adequate to capture the turbulent scales responsible for it. Overall the mean and fluctuating flow field structure are similar, except for the flow region comprised between $x/D = 0$ and $x/D = 1$.

3.3. Velocity structure function

As mentioned in Section 2, drop deformation results from spatial stress distribution at a scale comparable to its diameter (Eq. (6)). The goal here is to verify that the spatial structure of the turbulence seen by the drop is well reproduced by the simulations. Therefore, the evaluation and comparison with experiments of spatial correlations of velocity fluctuations at the drop scale, is an important step regarding DNS validation.

The drop diameter considered in the simulations equals 2.4 mm. At monitor point 2 ($x/D = 0.82$), the average axial velocity is $U_x = 0.25$ m s^{-1} and the frequency corresponding to the drop scale, $U_x/d \sim 10^2$ Hz, lies in the inertial subrange, which is accurately solved by the simulation. Further downstream, the grid has been progressively coarsened in the axial direction. In order
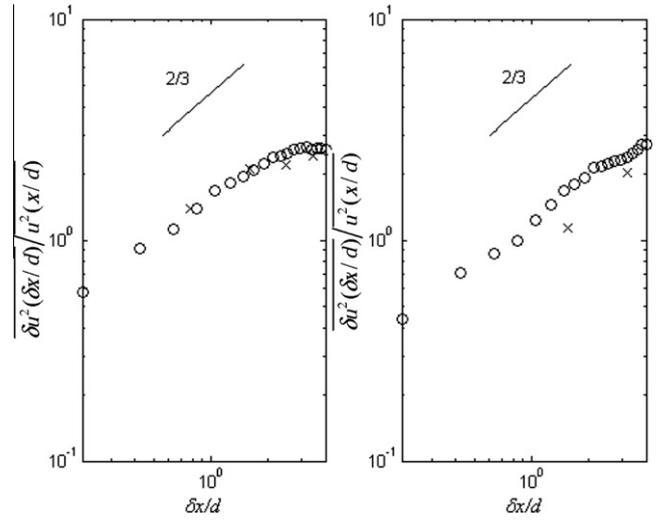

Fig. 9. Normalized structure function $\overline{\delta u^2(\delta x/d)}$. **o**: PIV experiments; **x**: numerical results. Left: point 1; right: point 4.

to check that accurate statistics of velocity fluctuations at the drop scale are obtained, the structure function of axial velocity fluctuation in the axial direction has been computed at the four locations x_i of the monitor points (cf. Fig. 1) and compared to experimental data. It is defined as

$$\overline{\delta u_x^2(x_i, \delta x)} = \overline{[u_x(x_i + \delta x) - u_x(x_i)]^2},\qquad(13)$$

where δx is a positive increment in x direction. In the case of locally isotropic turbulence, this quantity scales as $\delta x^{2/3}$ in the inertial range (Obukhov and Yaglom, 1953). This quantity is represented as a function of $\delta x/d$ in Fig. 9 and it can be concluded that the drop does experience velocity fluctuations within the inertial subrange. This is verified for all locations investigated (from point 1 to point 4). Although the pipe restriction produces a strongly inhomogeneous flow at large scale, the structure function follows the 2/3 power law as a function of separation distance δx. Simulation results closely follow experimental data at point 1 whereas the 2/3 power law scaling is preserved at point 4, located at 0.05 m from the orifice. The slight discrepancy observed at this point is related to the local mesh width, which is of the order of the drop diameter. At point 1, the ratio between the width of the mesh cell and the drop diameter is 0.7 whereas it increases to 1.4 at point 4.

In Fig. 4, we also compared numerical and experimental spatial distributions of the average turbulent Weber number based on $\overline{\delta u^2(x, d)}$, (Eq. (5)). The agreement is good both qualitatively and quantitatively when $x/D > 1$. The Weber number is continuously increasing downstream of the orifice section and reaches its maximum at $x/D = 1.5$. In the experimental data, the presence of moderate We numbers close to the orifice is due to large scale oscillations of the jet (see comments on Fig. 8 above).

The underlying assumption of Kolmogorov–Hinze theory of break-up in the inertial subrange is that the gradient of pressure fluctuation responsible for drop deformation is balanced by the local fluctuating acceleration at the scale of the drop. In homogeneous isotropic turbulence, it can be shown (Obukhov and Yaglom, 1953; Monin and Yaglom, 1975) that the quantity $\overline{\delta u^2(x, d)}$ would be equal to the square root of the pressure structure function multiplied by a factor 3

$$\rho_c \overline{\delta u^2(x, d)}_{HIT} = \rho_c \sum_{i=1}^3 \overline{\delta u_i^2(x, d)} \cong 3\sqrt{\overline{\delta P'^2(x, d)}_{HIT}}.\qquad(14)$$

Note that this equation is verified when the Re_λ is large enough (typically > 200). For lower values of Re_λ, the proportionality factor of Eq. (14) is expected to be larger (see Antonia et al., 1999). The right hand side term of Eq. (14) is most of the time not available experimentally. In return, it can be computed from the simulations. A Weber number based on the pressure structure function can therefore be computed according to

$$We_P = \frac{2\sqrt{\overline{\delta P'^2(x,d)}d}}{\sigma}. \tag{15}$$

Due to the absence of the third velocity component in the calculation of $\overline{\delta u^2(x,d)}$, a factor 2 here replaces the factor 3 of Eq. (14). The field of We_p is reported in Fig. 4 (right picture). A good qualitative agreement with the turbulent Weber number calculated from Eq. (5) (middle picture) can be observed. However, the two fields are not identical, We_p being smaller than We and a slight vertical shift between the two fields can be observed. The smaller value of We_p is consistent with the low value of Re_λ estimated in Eq. (4), but no quantitative scaling can be drawn between both quantities since the turbulent flow field is highly inhomogeneous. Nevertheless, we will see in next section that, for the purpose of predicting drop break-up, the turbulent contribution to the external forcing experienced from a drop can be evaluated from velocity fluctuations.

4. Simulation of drop deformation and breakup statistics

Individual drop trajectories downstream of the orifice have been simulated in a Lagrangian framework by solving the force balance (Eq. (16)) acting on an isolated drop:

$$\frac{dX}{dt} = \mathbf{v}; \quad \rho_d \frac{\pi d^3}{6} \frac{dv}{dt} = \mathbf{F}, \tag{16a}$$

$$F = (\rho_p - \rho_c)\frac{\pi d^3}{6}g + \rho_c V \frac{Du}{Dt} - \rho_c \frac{\pi d^2}{8} C_D |v-u|(v-u)$$
$$+ \rho_c \frac{\pi d^3}{6} C_M \left(\frac{Du}{Dt} - \frac{dv}{dt}\right) - \rho_c \frac{\pi d^3}{6} C_L (v-u)x(\nabla x u). \tag{16b}$$

In Eqs. (16), ρ_d, d, $\mathbf{X}$ and $\mathbf{v}$ are respectively the drop density, diameter, position and velocity vectors. d/dt and D/Dt are the material derivatives following the drop and the fluid respectively. $\mathbf{F}$ is the sum of buoyancy, drag, dynamic pressure gradient (also called Tchen force), added-mass and lift forces, while Basset contribution has been disregarded. Assuming that drops have a spherical shape, C_M is equal to 1/2 (Magnaudet et al., 1995). The drag coefficient is assumed to follow the classic Schiller and Naumann correlation. For high particulate Reynolds numbers (based on the slip velocity), the mechanisms that control lift effects are essentially of inviscid nature, so that the inviscid result $C_L = 1/2$ is appropriate. At lower Reynolds number, it was shown that C_L is a function of both the Reynolds number and the shear rate. In contrast, for Reynolds numbers typically less than unity, the situation becomes much more complex. This is why no general expression of the lift force applicable to an arbitrary linear flow field is available to date in this regime. We use the correlation proposed by Magnaudet and Legendre (1998). In the simulation of drop trajectories, the modulation of the flow field by the drop was neglected (dilute flow), and drops are considered as material points. The instantaneous velocity $\mathbf{u}$ and the velocity gradients involved in the force balance are provided through a local interpolation of the DNS flow field at the drop location. The system of ODEs (Eqs. (16)) has been efficiently solved with a four steps forward Runge–Kutta scheme. Examples of calculated trajectories are illustrated in Figs. 1 and 10.
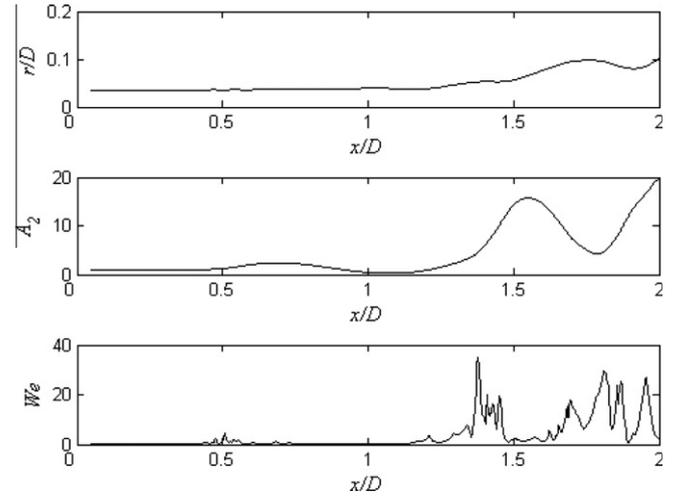

Fig. 10. Simulated drop trajectory (top figure), normalized amplitude of drop oscillation $\tilde{A}_2$ (middle figure) and instantaneous turbulent Weber number (bottom figure).

The Weber number is computed by DNS from the velocity fluctuation at the scale of the drop, which has been shown to be accurate from the examination of the structure functions (Fig. 8). It is a Lagrangian quantity since it is evaluated at the location $\mathbf{X}$ where the drop is at instant $\tilde{t}$. In order to compute it, the flow field is interpolated according to the drop position and the maximum value of $\delta u^2(\mathbf{X}(t),d)$ along four distinct directions is calculated, following Eq. (11) (for the sake of consistency with experiments, only the axial and radial components of the velocity have been accounted for in the computation of $\delta u^2(\mathbf{X}(t),d)$.

As aforementioned in Section 2, K is an unknown prefactor that is introduced to couple the dynamics of the drop shape with the turbulent forcing. Because Eq. (12) is linear, the value of K can be set arbitrarily to unity without loss of generality (A_2 is simply replaced by A_2/K). Eq. (12) has been solved numerically using a four-step forward Runge–Kutta scheme and considering that each drop was initially spherical and at rest ($\tilde{A}_2 = 0$ and $\frac{d\tilde{A}_2}{dt} = 0$).

Fig. 10 illustrates an example of simulation: the radial drop location r, the computed deformation A_2/K and the corresponding turbulent forcing We are plotted versus the axial location x/D. It is worth pointing out the differences between the turbulent forcing and the deformation which results from it: the evolution of A_2 is smoother than that of We, which indicates that the shape dynamics preferentially responds to frequencies close to f_2 and filters out higher turbulent frequencies. Moreover, local minima or maxima of A_2 do not coincide with those of We. As already observed by Galinat et al. (2007b), a break-up criterion based upon a threshold Weber number value is therefore not relevant. Following their observations, it will be assumed that breakup occurs when the computed deformation A_2 exceeds a critical value A_{2cr}. It is important to note that A_{2cr} is the only adjustable parameter of the model.

Trajectories and deformations of 450 drops have been simulated. Calculated breakup locations have been reported in Fig. 7 and show a good qualitative agreement with experimental data. In order to compare break-up statistics, cumulative distribution function $P(x/D)$ has been calculated from the simulations (probability that a drop breaks in the spatial domain [0, x/D]. $P(x/D)$ increases from zero at the orifice ($x/D = 0$) to a maximum value, which characterizes the break-up probability of a drop of this diameter after passing through the orifice.

Fig. 11 displays axial evolutions of $P(x/D)$ computed with four different critical deformations: $A_{2cr}/K = 14$, 15, 16 and 17. The experimental curve (thick line) nicely lies in between the cases corresponding to $A_{2cr}/K = 15$ and 16. Regarding the moderate
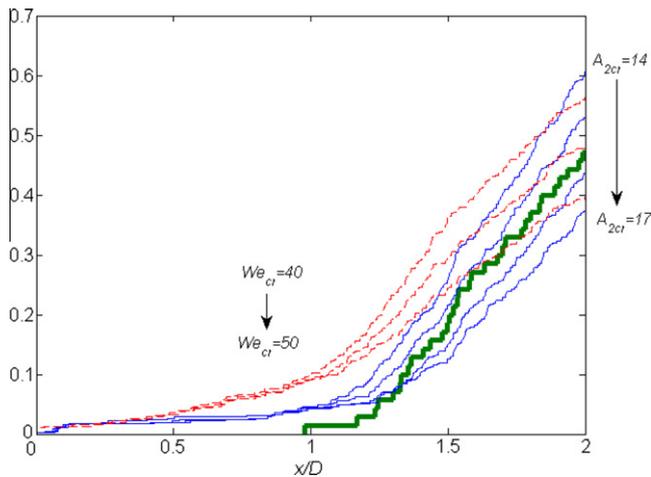
Fig. 11. Break-up probability versus the distance from the orifice. Thick continuous line: experiments; thin continuous lines: simulations assuming critical deformation values between 14 and 17; dotted lines: simulations assuming critical Weber values between 40 and 50.

number of samples considered in the experiments (70), this agreement is remarkable and tends to prove that the present dynamical model of drop deformation accounts for the right physical mechanism: the drop shape responds as an oscillator defined by its frequency and its damping rate. This dynamics also explains the occurrence of some break-up events located in regions of weak turbulence, as observed in Fig. 4.

$P(x/D)$ has also been calculated using a fragmentation criterion based on a critical value of the instantaneous Weber number (We_c). In Fig. 11, the corresponding curves have been also reported. The best fit of the maximum value is observed for We_c values ranging between 40 and 50. However, these curves drastically overestimate experimental results in the interval $0.5 < x/D < 1.5$, confirming that the drop deformation does not follow instantaneous turbulent fluctuations. It is also worth to notice that the order of magnitude of these critical values of the instantaneous Weber number is much larger that of the global Weber number based on an averaged dissipation rate (Eq. (1))

$$\overline{We} = \frac{\rho_c (1.4(\varepsilon d)^{\frac{1}{3}})^2 d}{\sigma} = 2\left(\frac{d}{D}\right)^{\frac{2}{3}} \frac{\rho_c U^2 d}{\sigma} \sim 0.9. \qquad (17)$$

Such a difference validates the coupling between the local turbulent forcing and the drop deformation dynamics to correctly describe the physics of fragmentation.

From video analysis of the experimental drop shape at the instant of breakup, Galinat et al. (2007a) estimated that the critical deformation A_{2cr} was approximately unity. Best agreement between experiments and present simulations is obtained for $A_{2cr}/K = 16$, leading to $K = 0.06$. This estimation is close to the value $K = 0.04$ obtained by Galinat et al. (2007a) by solving Eq. (12) using a forcing term $We(t)$ obtained from PIV measurements in a single radial plane and by computing drop motions assuming a constant drift velocity relative to the liquid.

5. Conclusion

Drop breakup in the turbulent inhomogeneous flow that develops downstream of an orifice has been numerically modeled by coupling DNS simulations of the continuous phase, Lagrangian droplet tracking, a dynamic model of drop deformation and a break-up criterion based on a maximal deformation. The dynamical model is adapted from the Kolmogorov–Hinze theory of turbulent break-up to the Rayleigh–Lamb theory of drop oscillations as already

proposed by Risso and Fabre (1998). Compared to PIV measurements, DNS results have demonstrated to provide a reliable prediction of the turbulent flow field and its statistics at the drop size scale. Experimental break-up locations have been correctly predicted by adjusting only one single parameter in the numerical model: the critical deformation $\tilde{A}_{2cr}$ for breakup. The ability of the forced oscillator to predict turbulent drop break-up in a non-homogeneous turbulent flow field has been tested and discussed. The model involves a prefactor K that has not been derived from theoretical consideration so far. However, once K has been fixed empirically by comparison with experiments, the proposed model can be tested for the prediction of local breakup probability in an inhomogeneous unsteady flow. These simulations can also be used to study the response of different drop diameters and different liquid/liquid systems as well, i.e. with different damping rates and frequencies.

References

Abi Chebel, N., 2009. Interfacial Dynamics and Rheology of an Oscillating Drop at High Frequency. PhD Thesis, INP Toulouse.
Antonia, R.A., Bisset, D.K., Orlandi, P., Pearson, B.R., 1999. Reynolds number dependence of the second-order turbulent pressure structure function. Phys. Fluids 11, 241–243.
Becker, H.A., Massaro, T.A., 1968. Vortex evolution in a round jet. J. Fluid Mech. 31, 435–448.
Furuichi, N., Takeda, Y., Kumada, M., 2003. Spatial structure of the flow through an axisymmetric sudden expansion. Exp. Fluids 34, 643–650.
Galinat, S., Masbernat, O., Guiraud, P., Dalmazzone, C., Noik, C., 2005. Drop break-up in turbulent pipe flow downstream of a restriction. Chem. Eng. Sci. 60, 6511–6528.
Galinat, S., Risso, F., Masbernat, O., Guiraud, P., 2007a. Dynamics of drop breakup in inhomogeneous turbulence at various volume fractions. J. Fluid Mech. 578, 85–94.
Galinat, S., Garrido Torres, L., Masbernat, O., Guiraud, P., Risso, F., Dalmazzone, C., Noik, C., 2007b. Break-up of a drop in a liquid–liquid pipe flow through an orifice. AIChE J. 53, 56–68.
Hinze, J.O., 1955. Fundamentals of the hydrodynamic mechanism of splitting in dispersion processes. AIChE J. 1, 289–295.
Kolmogorov, A.N., 1949. On the disintegration of drops in a turbulent flow. Dokl. Akad. Nauk 66, 825–828.
Lamb, H., 1932. Hydrodynamics. Cambridge University Press.
Lasheras, J.C., Eastwood, C., Martínez-Básan, C., Montañés, J.L., 2002. A review of statistical models for the breakup of an immiscible fluid immersed into a fully developed turbulent flow. Int. J. Multiph. Flow 28, 247–278.
Lu, H.L., Apfel, R.E., 1991. Shape oscillations of drops in the presence of surfactants. J. Fluid Mech. 222, 351–368.
Macagno, E.O., Hung, Tin-Kan, 1967. Computational and experimental study of a captive annular eddy. J. Fluid Mech. 28, 43–64.
Magnaudet, J., Rivero, M., Fabre, J., 1995. Accelerated flows past a rigid sphere or a spherical bubble. Part I: steady straining flow. J. Fluid Mech. 284, 97–135.
Magnaudet, J., Legendre, D., 1998. Some aspects of the lift force on a spherical bubble. Appl. Sci. Res. 58, 441–461.
Martínez-Bazán, C., Montañés, J.L.T., Lasheras, J.C., 1999. On the breakup of an air bubble injected into a fully developed turbulent flow. Part 1. Breakup frequency. J. Fluid Mech. 407, 157–182.
Merle, A., Legendre, D., Magnaudet, J., 2005. Forces on a high-Reynolds-number spherical bubble in a turbulent flow. J. Fluid Mech. 532, 53–62.
Miller, C.A., Scriven, L.E., 1968. The oscillations of a fluid droplet immersed in another fluid. J. Fluid Mech. 32, 417–435.
Monin, A.S., Yaglom, A.M., 1975. Statistical Fluid Mechanics, vol. 2. MIT, Cambridge.
Morrison, G.L., DeOtte, R.E., Nail, G.H., Panak, D.L., 1993. Mean velocity and turbulence fields inside an orifice flowmeter. AIChE J. 39, 745–756.
Mullin, T., Seddon, J.R.T., Mantle, M.D., Sederman, A.J., 2009. Bifurcation phenomena in the flow through a sudden expansion in a circular pipe. Phys. Fluids 21, 014110.
Obukhov, A.M., Yaglom, A.M., 1953. The microstructure of turbulent flows. NACA, Tech. Mem. 1350, 1–41.
Prosperetti, A., 1980. Normal-mode analysis for the oscillations of a viscous drop in an immiscible liquid. J. Mécanique 19, 149–182.
Risso, F., Fabre, J., 1998. Oscillation and breakup of a bubble immersed in a turbulent field. J. Fluid Mech. 372, 323–355.
Risso, F., 2000. The mechanisms of deformation and breakup of drops and bubbles. Multiph. Sci. Technol. 12, 1–50.